Chapter 4

Magnetic soft x-ray scattering at the Ho M_V absorption threshold

Ho metal has played an important role as a reference system in the development and understanding of magnetic and resonant magnetic x-ray scattering. The first observation, e.g., of resonant magnetic x-ray scattering in an antiferromagnet was made on Ho. Ho exhibits a nearly perfect helical magnetic structure across a wide temperature range which can be described by a single modulation vector. This makes the data interpretation relatively simple since higher-order magnetic reflections must arise from non-linear terms in the scattering amplitude, rather than from higher Fourier components of the magnetic structure. The long modulation periods produce scattering signals that are fairly close to neighboring lattice reflections, but usually do not overlap with them. The bulk magnetic structure of Ho metal has been studied intensively using the resonant enhancement of the magnetic-scattering amplitude at the Ho L_{III} absorption threshold [81, 83, 101]. Furthermore, it was shown that magnetic scattering at the L_{III} absorption threshold is also suitable to explore the magnetic structure of Ho films down to a thickness of about 100 monolayers, in which an essentially bulk-like behavior was found [53, 90]. But despite the enhancement of the magnetic-scattering amplitude, and the high photon flux with a high degree of polarization available at third-generation synchrotron-radiation facilities, it was not possible to study the magnetic structure of thinner films in a thickness range, where finite-size and strain-induced effects are expected. The experimental problems are schematically illustrated by the simulations in figure 4.1 for three different film thicknesses. The simulation is based of the experimentally obtained contrast between magnetic and charge scattering after polarization analysis from the lower spectrum in figure 2.7. Despite the remaining charge-scattering background, the magnetic scattering signal can be separated clearly in case of the 100-ML film. A reduction of the film thickness, however, leads to a broader intensity distribution in momentum space of all peaks according to equation 2.6. While the peak height of the magnetic satellites goes rapidly down with decreasing film thickness, the charge-scattering background stays nearly constant at the magnetic satellite position making the experimental observation of the magnetic signal more and more difficult. Already for a 30-ML Ho film, the magnetic signal will be hard to observe, as experimentally

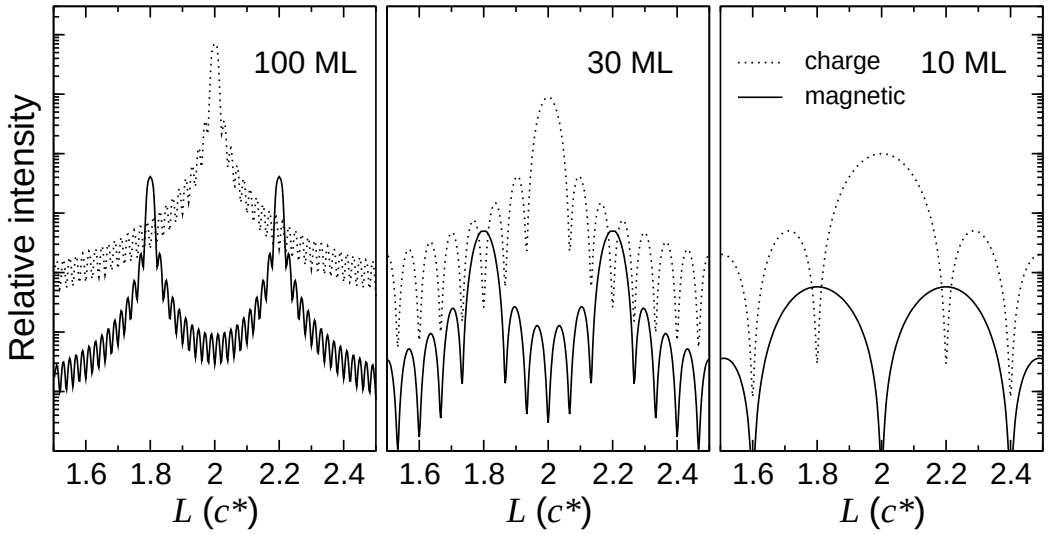

Figure 4.1: Simulation of magnetic scattering from Ho films with different film thicknesses at the Ho L_{III} absorption threshold using polarization analysis. The contributions of magnetic (solid lines) and charge scattering (dotted lines) are displayed separately for each film thickness. The achievable contrast between magnetic and charge contribution is deduced from the experimental data shown in figure 2.7.

shown in reference 53. For even thinner films, this technique is not applicable any more.

The properties of resonant scattering are determined by the intermediate states involved in the scattering process. At the lanthanide $L_{II,III}$ resonances these are the $s-$ and $d-$like valence states, which are only polarized by the local $4f$ moment. Thus, the lanthanide $L_{II,III}$ absorption threshold exhibit a modest dichroism and an enhancement of the magnetic-scattering intensity by 1-2 orders of magnitude [81]. Dipole-allowed excitations to intermediate states, which are sharper in energy and of higher polarization, would be desirable for magnetic-scattering experiments. The most appealing states in this respect are the $3d$ bands in $3d$-transition metals, the $4f$ states of the lanthanides, and the $5f$ states of the actinides, since these states exhibit a large exchange splitting and are responsible for magnetism in the respective elements or compounds.

For the $M_{IV,V}$ resonances of the lanthanides and actinides, it has been predicted that the usually small magnetic contributions to the scattering amplitude can be of the same order of magnitude as the charge scattering amplitudes [84]. Thus, one of the most exciting discoveries in magnetic x-ray scattering was the experimental observation of the huge resonant enhancement of the magnetic signal by six to seven orders of magnitude at the uranium M_{IV} absorption threshold ($3d-5f$ transition) [102, 103]. While for the actinides, the $M_{IV,V}$ resonances occur at photon energies above 3 keV, the other interesting excitations occur within the soft x-ray region with corresponding wavelengths, which are too long for crystal diffraction, but are well suited for a wide variety of long-period structures e.g. long-period antiferromagnets (as shown in the present work), systems with charge or orbital order [104, 105], or artificial systems like multilayers and nanostructures. In the

present case, the wavelengths at the Ho M_V threshold of 9 - 9.5 Å match well the magnetic period length of about 20 to 28 Å.

Resonant magnetic soft x-ray scattering is a comparably new technique providing the unique properties that are required to study the magnetic structures of ultrathin lanthanide-metal films. While the magnetic structures of thin and ultrathin films are the subject of the subsequent chapters, the present chapter deals with the characterization of the scattering process at the Ho M_V absorption threshold itself. Ho metal films are a good choice to characterize the method mainly for two reasons. Firstly, the magnetic structure of bulk Ho is well known, and sufficiently thick Ho-metal films are known to have a bulk-like magnetic structure. Secondly, Ho films can be prepared with a higher surface quality and much cleaner than bulk single crystals, either *in situ* or by MBE techniques, which is important for the interpretation of the comparably surface-sensitive soft x-ray scattering results.

4.1 Optical parameters

In the x-ray region, the index of refraction $n = 1 - \delta + i\beta$ is usually close to unity, and thus in most x-ray scattering experiments it is not necessary to take absorption and dispersion into account. But at strong resonances, like the $M_{IV,V}$ absorption thresholds of the lanthanide metals, changes in the optical parameters are considerable and must be taken into account in any quantitative analysis. X-ray optical parameters are well known off resonance and tabulated in reference 106. At resonance, however, the optical parameters are often unknown, even for standard materials.

Various methods are used to determine the optical parameters. A common method is to determine the imaginary part of the index of refraction, β, from absorption measurements, scaled to tabulated off-resonance data far away from the absorption threshold. The real part, δ, can then be calculated from the imaginary part via Kramers-Kronig transformation [107]. The problem of this method is that systematic errors of absorption measurements are difficult to avoid. Total-electron yield, which is a widely-used technique, is proportional to the absorption coefficient only in the limit of a wavelength being much larger than the probing depth [108, 109]. Transmission experiments that directly measure the absorption are often disturbed by the absorbing substrate foil, by inhomogeneities of the films, and by uncertainties about the film thickness [109]. Furthermore, the scaling of the weak off-resonance absorption signal values to reference data depends critically on the proper consideration of background intensities, often leading to systematic errors. Few experiments have been performed to determine the real part of the index of refraction, δ, at resonance directly, by measuring the Bragg-peak displacement when the photon energy is scanned through an absorption threshold. There are even less efforts to obtain both β and δ from the same experiment by means of a combination of Bragg scattering and absorption measurement [110–112], or by making use of the Faraday effect in magnetic materials [112, 113]. In the present study, the optical parameters were determined directly and without adjustable parameters by fits of a dynamical model to reflectivity curves,

including the magnetic-superstructure peak.

Resonant magnetic scattering at the M_V absorption threshold of Ho does not require a polarization analysis to extract the magnetic signal as it is necessary in the conventional x-ray region. Because of a huge resonant enhancement of the magnetic-scattering cross section, which will be quantified in the following, it is possible to achieve a pronounced magnetic signal only by tuning the photon energy to the M_V absorption threshold. As an example, profiles of the reflectivity and the magnetic satellite recorded at three different photon energies from a 110-ML Ho film are presented in figure 4.2. The figure shows the scattered intensity as a function of momentum transfer perpendicular to the surface, $q_\perp$, and parallel to the surface, $q_\parallel$, on a linear scale. These data represent sets of rocking scans (fits) taken at various values of $q_\perp$. At 900 eV, well below the absorption threshold, the magnetic signal is too weak to be observable on a linear scale. The profile shows Kiessig fringes along the $q_\perp$ direction centered at $q_\parallel = 0$, typical for a thin film on a substrate as discussed in section 2.1. Off specular, in $q_\parallel$ direction, the intensity falls off rapidly. The shape along $q_\parallel$ for all $q_\perp$values can be described essentially by a Lorentzian line shape with a constant width corresponding to the inverse in-plane coherence length of the film. By tuning the photon energy closer to the resonance ($h\nu = 1330$ eV), which is still 24 eV below the resonance maximum, the (000+τ) magnetic satellite appears and becomes the dominating structure. Near the resonance maximum at 1350 eV, the magnetic satellite gains even more intensity and becomes broader; also the Kiessig fringes are smeared out at this energy. Both, the broadening of the magnetic satellite and the damping of the Kiessig fringes are caused by the reduced penetration depth of the photons near the resonance maximum, as will be discussed later. An important information is the fact that also the rocking-curve width of the magnetic satellite, $W_{q,\parallel}$, does not change with $q_\perp$. Hence, the total integrated intensity of the magnetic satellite is proportional to the intensity integrated along $q_\perp$, and a one-dimensional model can be applied to describe the spectra.

A set of specular x-ray reflectivity scans from the same film at various photon energies is shown in figure 4.3. In a conventional x-ray scattering experiment, a kinematical model is usually sufficient to describe the data, as long as the scattering angles are well above the critical angle. Such a description will fail here because of the strong photon absorption at the M_V resonance, and a dynamical model has to be applied for both, the reflectivity and the magnetic satellite. This was done by introducing absorption and dispersion corrections into the structure factor of the helical magnetic superstructure [80] so that the scattered intensity along $q_\perp$ can be written as

$$I\left(q_\perp\right) \propto \left| P \cdot e^{-\frac{1}{2}q_\perp^2 \sigma_{rms}^2} \cdot \sum_{n=0}^{N-1} e^{ind(q_\perp - \tau)} \right|^2 , \tag{4.1}$$

where the Debye-Waller type damping factor describes the roughness, N is the number of layers contributing to the scattering signal, $d = c/2$ is the layer spacing along the crystallographic c axis and τ denotes the absolute value of the magnetic modulation vector. In case of magnetic scattering, the polarization factor P depends on the individual magnetic structure as well as on the individual scattering geometry as discussed in section 2.2.

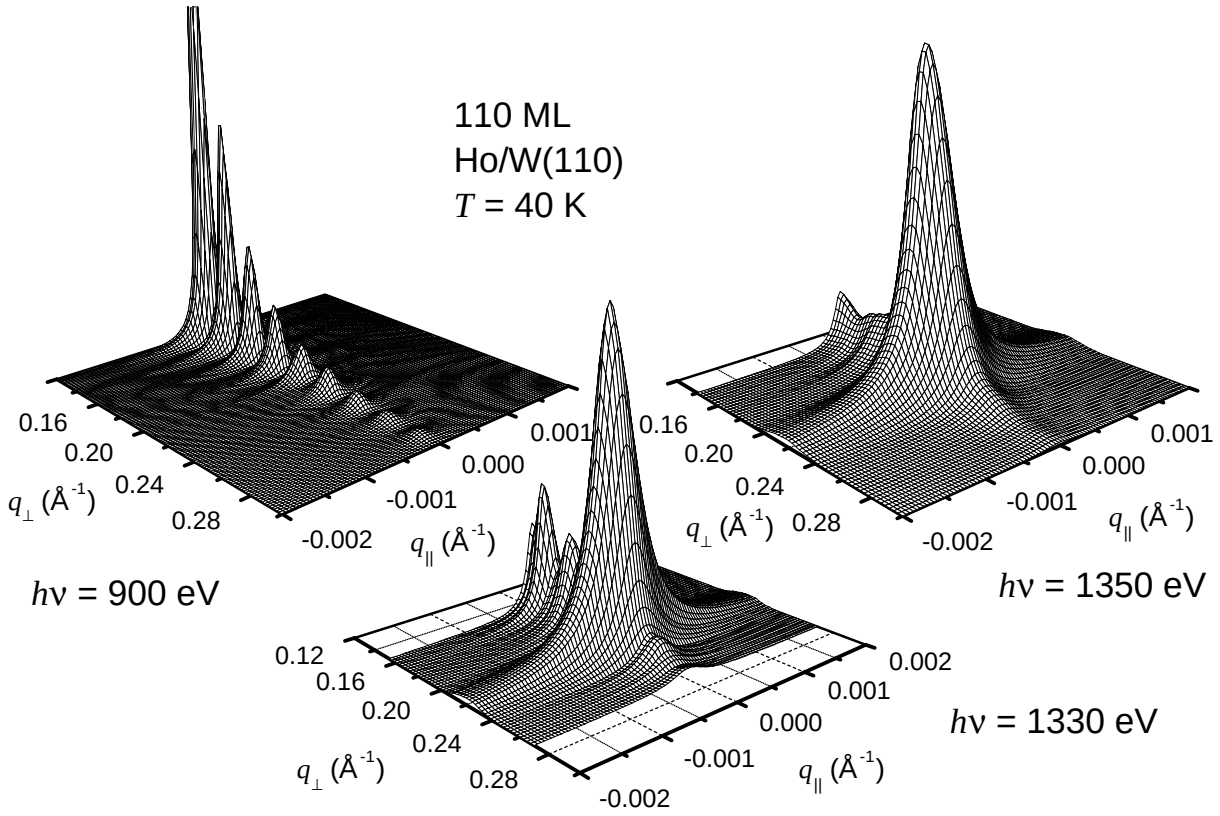

Figure 4.2: Reflectivity profiles of a 110-ML Ho film grown on W(110) as extracted from sets of rocking scans. The leftmost spectra are obtained far below resonance at $h\nu = 900$eV, the spectra on the right near the resonance maximum at 1350 eV, and the spectra in the center at the foot of the resonance at 1330 eV. $q_\perp$ is the perpendicular component of the scattering vector along the surface normal and $q_\parallel$ denotes the in-plane component.

Absorption and dispersion correction are introduced in analogy to the theory of reflectivity by a complex momentum as described in section 2.1

$$q_\perp = \frac{4\pi}{\lambda} \cdot \sin\left(\sqrt{\widetilde{\Theta}^2 - 2\delta + i2\beta}\right),$$

where $\widetilde{\Theta}$ denotes the scattering angle in specular scattering geometry with respect to the sample surface, δ and β are the real and imaginary part of the index of refraction, respectively. The spectra were analyzed as a superposition of a magnetic satellite as given by equation 4.1 and a background from charge scattering described by a dynamical theory of reflectivity (section 2.1).

Charge-magnetic interference effects are expected to be small, and were neglected for reasons discussed in the following. In the non-resonant limit, the magnetic-scattering amplitude for linearly polarized radiation is 90° out of phase with the charge scattering amplitude. This phase shift prevents interference between magnetic and charge scattering.

Also in case of resonant magnetic scattering from AFM systems, interference can usually be neglected because the magnetic and charge scattering signals are well separated in momentum space. In systems like ferromagnets, where the magnetic and charge scattering contributions overlap, an interference term occurs in the resonant-scattering cross section with a complicated energy dependence. The oscillator strengths F_ζ^1 (see equation 2.9) are in general complex, hence both the magnetic and the charge scattering amplitude are complex with strongly energy-dependent phases, thus interference will appear with different strength across the resonance. Magnetic-charge interference scattering, however, is hard to observe even in ferromagnets and has been achieved in only a few cases [83,114,115]. While for FM systems, the charge- and magnetic-scattering signal appears at the same points in momentum space, in AFM thin films, the charge scattering signals at the magnetic-peak positions are small and only present in the Kiessig fringes or Laue oscillations. Additionally, only a fraction of the magnetically-scattered signal preserves the polarization direction of the incoming beam required to interfere with the charge scattering signal, as can be seen from the polarization factors in equation 2.10. The best fit results, indeed, have been achieved without any interference, which is therefore neglected in the following.

With the model described above, spectra of a sufficiently simple system like a homogeneous film on a semi-infinite substrate can be described in detail, as shown in figure 4.3. The results of the sample fits are plotted as solid lines through the data points. The subspectra correspond to the magnetic (dashed line) and the charge-scattering contribution (dotted line), respectively.

At a photon energy of 900eV, the magnetic signal can be observed even on a logarithmic scale only as a less pronounced minimum of the Kiessig fringes. Using the optical parameters of Ho and W as known from literature [106], which are reliable far off resonance, the 900-eV data could be readily fitted, providing the structural parameters thickness and roughness of the film. Near resonance, at 1340eV, a well-pronounced magnetic satellite can be seen in the scan. The Kiessig fringes are damped, because the penetration depth of the photons is now comparable to the film thickness. Knowing the structural film parameters, the optical parameters are determined from the shape of the Kiessig fringes, and thus it is possible to determine the magnetic-modulation vector and the number of magnetically ordered atomic planes from the magnetic signal. The parameters of the magnetic structure can be refined iteratively by describing all spectra across the resonance. The number of magnetically ordered monolayers obtained from the magnetic signal compared to the film thicknesses extracted from the Kiessig fringes shows that the magnetic structure is present over the whole thickness of this epitaxially grown film. A consistent description, however, requires the introduction of a separate magnetic roughness, larger than the structural roughness. Typical values of the root-mean-square roughness, σ_{rms}, as obtained from the fits are 0.5 - 3 Å for the combined surface and interface roughness and 2 - 5 Å for the magnetic roughness. A possible deviation of the structural from the magnetic roughness has been reported earlier, and both cases have been found: magnetic structures that are smoother and such that are rougher than the interface [116–118].

After determination of the structural parameters, which are not energy dependent, the only remaining energy-dependent parameters are the optical constants δ and β and the

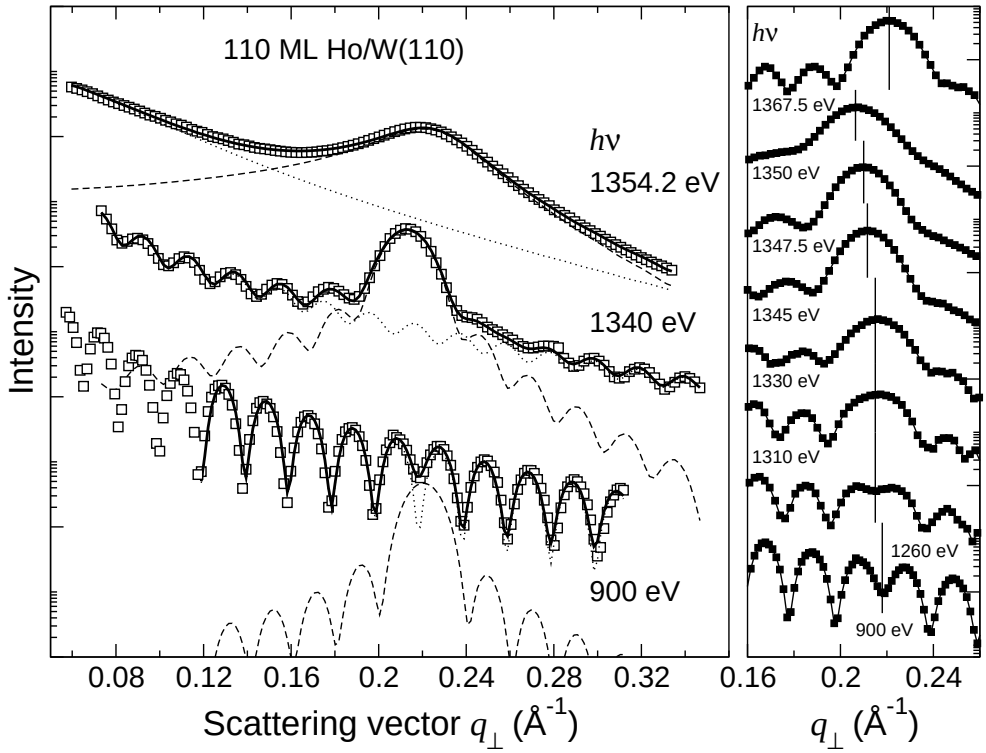

Figure 4.3: X-ray reflectivity scans of a 110-ML Ho film at various photon energies. In the left panel, examples of the data analysis are shown. The solid lines through the data points represent least-squares fit analyses as described in the text. The subspectra correspond to the magnetic (dashed) and charge contribution (dotted). The right panel demonstrates the strong refractive effects across the resonance. The vertical bars mark the position of the magnetic satellite. For illustration, the data have been multiplied leading to vertical offsets on a logarithmic scale.

intensities due to the change of magnetic- and charge-scattering cross section. The model works for all photon energies across the resonance, also close to the resonance maximum, where the reduced x-ray penetration depth leads to broad, structureless shapes as shown in the topmost spectrum in figure 4.3.

Figure 4.4 summarizes the results of this analysis, obtained from two different Ho films. The x-ray absorption signal (XAS) measured by the sample drain current from a 31-ML Ho film is displayed on the upper panel. It shows a multiplet structure corresponding to the $3d^{10}4f^{10} \rightarrow 3d^{9}4f^{11}$ electronic excitations with essentially three main components, which will be identified later. The optical parameters have been obtained from the 31- (circles) and a 110-ML Ho film (squares). The absorptive part of the index of refraction, β (filled symbols in panel (b)), has its maximum at the same energy position and with roughly the same width as the XAS. The dispersive part, δ, is displayed in the same plot (open symbols). It shows a typical resonance behavior and is in good agreement with the Kramers-Kronig transform of the absorptive part, β, shown as the thick line in the same

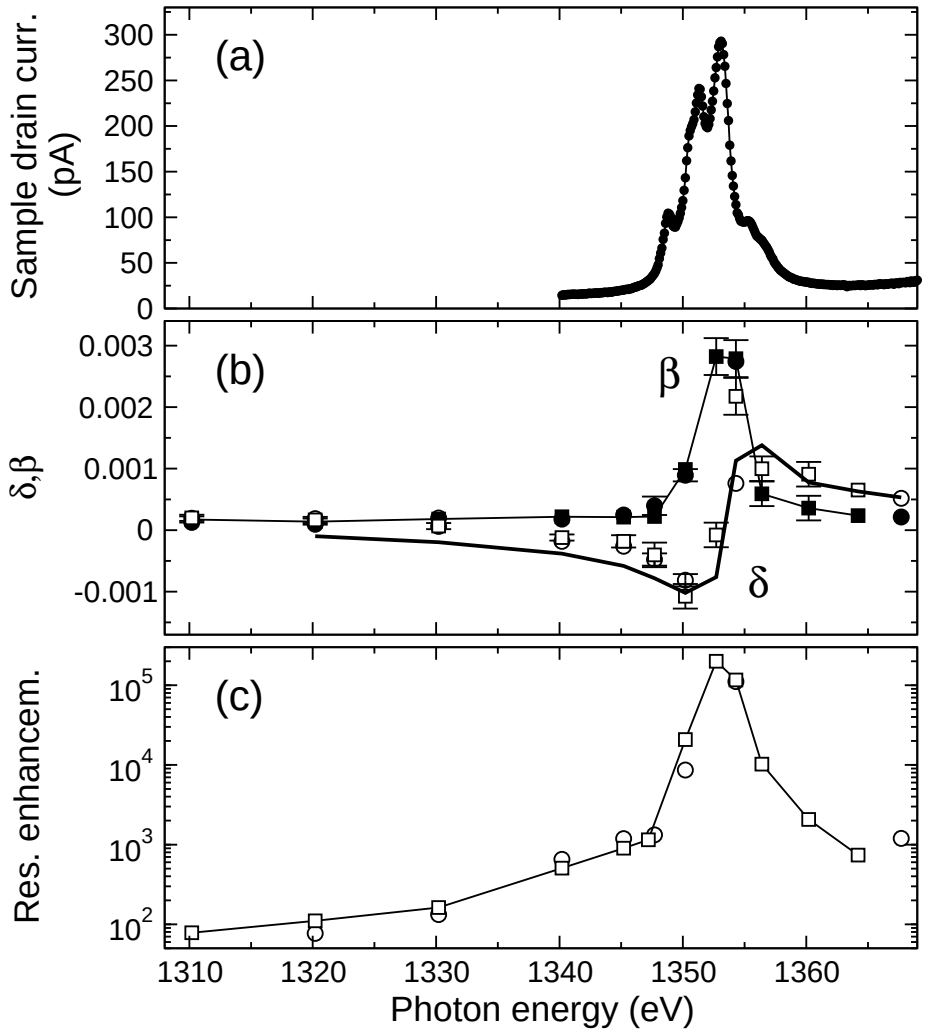

Figure 4.4: (a) X-ray absorption spectrum recorded by the sample drain current from a 31-ML Ho film as a function of photon energy. (b) Optical parameters δ and β of Ho across the M_V absorption threshold as extracted from reflectivity fits of a 110- (squares) and 31-ML Ho film (circles). The thick solid line (δ) represents the Kramers-Kronig transform of the absorptive part β. (c) Resonant enhancement of the magnetically scattered intensity across the M_V absorption threshold. The data are normalized to the intensity obtained at 900 eV photon energy.

panel.

The maximum value of β (0.0028 ± 0.0003) is smaller by a factor of about 1.8 than a value derived from x-ray transmission experiments from Ho films on Mylar foils as given by reference 109. As stated by the authors, their absolute values might be affected by systematic errors. On the other hand, by using the relative values of the absorption coefficients of Gd and Ho given in reference 109, the data could be compared to the Gd data presented in reference 119. In that case, the agreement is very good.

The integrated satellite intensity is another free parameter in the fit model above. Its variation is a measure of the change of the magnetic-scattering cross section. But due to the strong variation of the photon penetration depth across the resonance, the probed volume changes with photon energy, and thus the measured intensities do not reflect the change of the magnetic-scattering cross section directly. To extract a resonant enhancement of the magnetic-scattering cross section, an absorption correction is required. The correction factor has been determined for each photon energy by a calculation of the dynamical magnetic structure factor (equation 4.1) using the experimentally obtained values for τ, N, β, and δ. The corrected integrated intensities are shown in the lower panel of figure 4.4. The data are normalized to the integrated intensity measured off resonance at 900 eV. Compared to this value, the magnetic-scattering signal is enhanced by a factor of more than 10^5. But even 450 eV below the absorption threshold at 900 eV the magnetic satellite is still detectable without use of polarization analysis. The above-mentioned enhancement of six to seven orders of magnitude, found for the satellite intensity of AFM UAs at the U M_{IV} absorption threshold was described by the same quantity: the relative change of the scattered intensity as compared to the intensity at about 1300 eV away from the maximum of the M_{IV} absorption threshold. The obtained number is of practical interest, but strongly dependent on the choice of the reference energy. Of more importance is the determination of the absolute magnetic-scattering cross section and the comparison to expected resonance and off-resonance values. This will be worked out in the following section.

4.2 Differential magnetic-scattering cross section

At the resonance maximum, the absorptive part of the index of refraction, β, corresponds to a photon absorption length of about 240 Å, which - due to the small angle of observation of the magnetic satellite - corresponds to an effective absorption depth of about 25 Å along the normal of the sample surface. To keep absorption corrections small, the differential scattering cross section was studied for a Ho film with a thickness of only 42 Å (corresponding to 16 monolayers), where a reasonable scattering intensity can still be expected. The film was embedded between Y layers, leading to a shift of the magnetic modulation vector to larger values, for reasons that are discussed further below in chapter 5. This shift helps for a better separation of magnetic and charge scattering contributions, and in this way allows to determine the magnetically scattered intensity and thus the differential magnetic-scattering cross section very reliably.

Figure 4.5 shows reflectivity scans recorded at various photon energies from this film. In the single spectrum on the left first- and second-order satellites are clearly visible, sitting on a charge-scattering background that is more complicated than that of a Ho/W(110) film due to the more complicated layer structure of the sample. The whole set of spectra across the M_V absorption threshold is displayed in the gray-scale plot on the right side of figure 4.5, where dark represents high intensity. The upper part of the figure is shown on a different gray scale than the lower part in order to better visualize the weak second-order satellite. Both satellites show a resonance behavior, but peak at different photon energies as seen

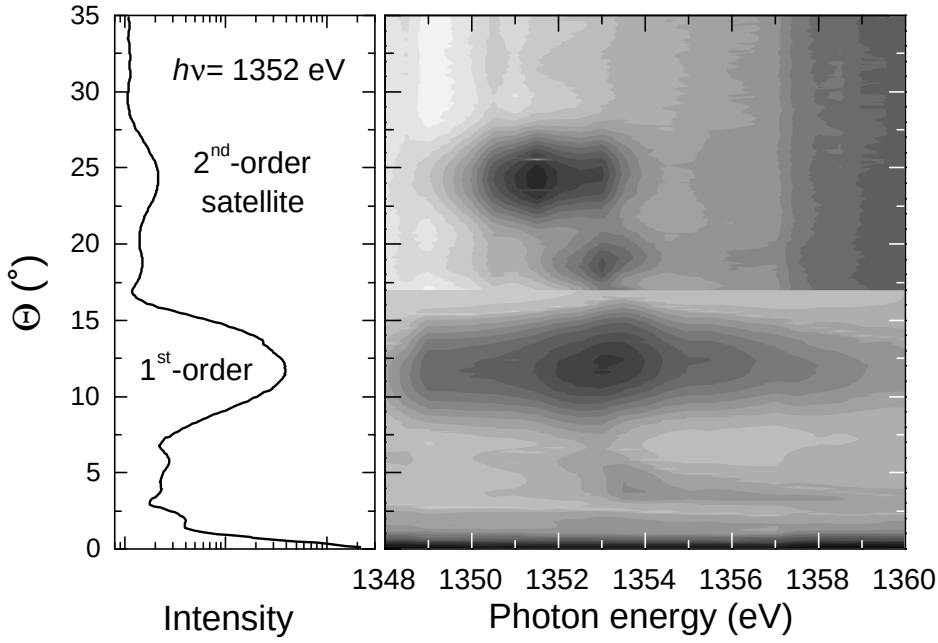

Figure 4.5: Specular x-ray reflectivity scans measured from a 16-ML Ho film as a function of photon energy. The exemplary spectrum shown in the left panel was recorded with 1352-eV photons and shows clearly visible first- and second-order magnetic satellites. All spectra measured are included in the contour plot given in the right panel on a logarithmic scale; darker colors represent higher intensities. The upper part of the plot is shown on a different scale than the lower part to visualize the second-order satellite.

in the bottom panel of figure 4.6. In contrast to the first-order satellite, the second-order satellite resonates only in a rather narrow energy interval and is not detectable outside. This illustrates the purely resonant nature of the second-order satellite, different from the first-order satellite, which is also present off-resonance.

The variation of the integrated intensities of the two satellites as a function of photon energy can be clearly assigned to different components of the $3d \rightarrow 4f$ x-ray absorption spectrum of Ho as displayed in figure 4.6 (a). Its behavior can be understood by looking at the variation of the dichroic character across the absorption threshold referring to the components in the resonant-scattering amplitude (equation 2.9). The M_V absorption spectrum of a Ho^{3+} ion can be decomposed into three components, representing optical transitions according to the dipole selection rule $\Delta J = 0, \pm 1$ [120, 121]. In a magnetic field, a partial lifting of the degeneracy of the $4f$ sublevels takes place, leading to a magnetic polarization of the three partial spectra ΔJ at low temperatures. Depending on the photon spin and its projection onto the magnetic moment, transitions of $\Delta M_J = 0, \pm 1$ are possible. But only a few total final states $|J', M'_J\rangle$ can be reached via dipole transitions from the magnetic ground state $|J, M_J = -J\rangle$. The dominating contributions to the photon absorption are transitions that fulfill the condition $\Delta J = -\Delta M_J$ as identified by Thole *et al.* [108]. Thus, the selection rules for ΔJ can be essentially identified by those for ΔM_J, which en-

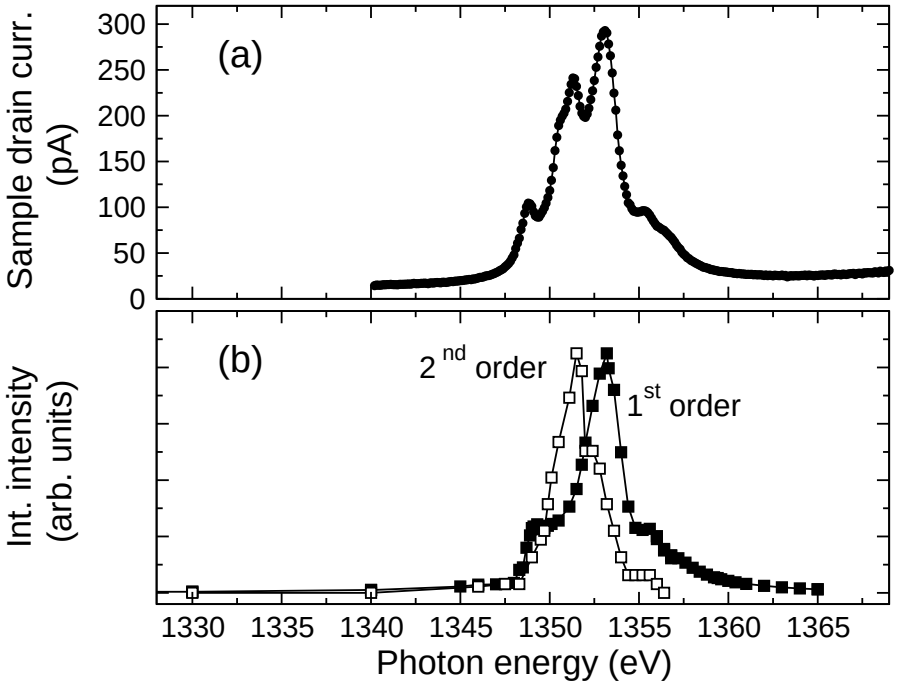

Figure 4.6: (a) X-ray absorption spectrum across the Ho M_V threshold from a 31-ML Ho film measured via the sample drain current. (b) Integrated intensities of the first-order (filled symbols) and second-order (open symbols) magnetic satellite as obtained from a 16-ML Ho film as a function of photon energy. The intensities of both satellites are shown on different scales.

ter equation 2.9. The XAS of Ho can be roughly decomposed into components of pairs of $(\Delta J; \Delta M_J) = (1; -1),\ (0; 0),\ (-1; 1)$ [120–122]. A fit of the main components, referring to the $\Delta J = 0, \pm 1$ subspectra as taken from reference 120 and broadened in order to account for lifetime and instrumental resolution is shown in figure 4.7(a). The first and the third component refer to transitions with $\Delta J = \pm 1$, which can be excited by left and right circularly polarized light, respectively. The component in the middle is of linear dichroic nature, referring to $\Delta J = 0$. The so identified components of the XAS can be compared to the resonant magnetic-scattering amplitude calculated for a magnetic helical structure (equation 2.10), which discloses that the first-order contribution is of purely circular-dichroic nature, while the second-order contribution is of purely linear-dichroic nature. Since both satellites are well separated in momentum space and have different dichroic character, the linear- and circular-dichroic contributions to the scattered intensity, and thus to the differential magnetic-scattering cross section, can be readily separated in resonant magnetic scattering.

Having understood the dichroic character of the involved excitations, we now turn to the satellite intensities. Assuming a crystal with a one-atomic basis that is described by the momentum- and energy-dependent atomic form factor $f(E, \underline{q})$, the differential scattering

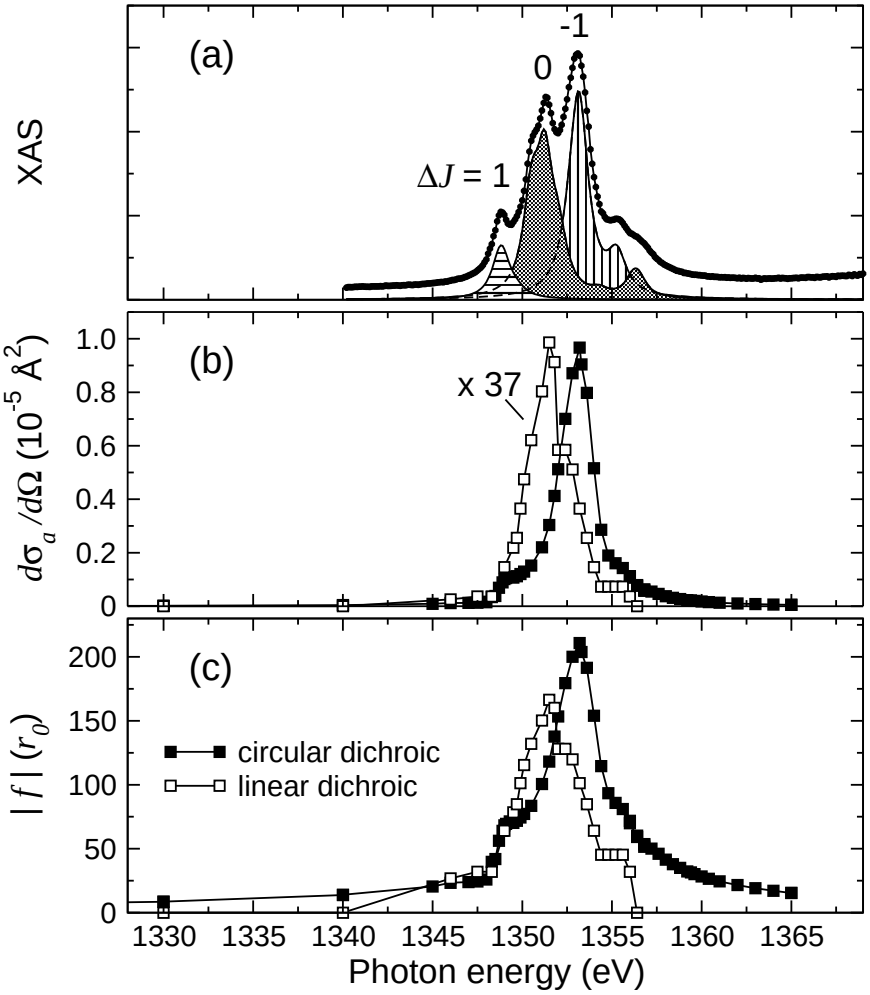

Figure 4.7: (a) X-ray absorption spectrum (XAS) across the Ho M_V absorption threshold measured by the sample drain current for a 31-ML Ho film. The subspectra represent the contributions of $\Delta J = 0, \pm 1$ to the XAS. (b) Differential magnetic-scattering cross section per atom as obtained from the first-order (filled symbols) and second-order magnetic satellite (open symbols). (c) Circular-dichroic (filled symbols) and linear-dichroic contributions (open symbols) to the atomic scattering amplitude near forward scattering in units of the classical electron radius r_0.

cross section can be written in general form as [67]

$$\frac{d\sigma}{d\Omega} = r_0^2 P^2 \left| f\left(E, \underline{q}\right)\right|^2 \left|F\left(\underline{q}\right)\right|^2,$$

with the classical electron radius r_0, the polarization dependence P, and the structure factor $F(\underline{q})$. Different from charge scattering, the polarization dependence in magnetic scattering is not only caused by the polarization states of the incident and scattered x-rays, but also by the relative orientation of the local magnetic moment with respect to these polarization

states (see equation 2.9). Thus, the differential magnetic-scattering cross section (DMSCS) depends strongly on the individual magnetic structure and scattering geometry. Therefore, a useful number, which can be compared to atomic calculations and which is independent of the specific experiment is the absolute value of the atomic form factor $|f(E, \underline{q})|$ that can be derived from the DMSCS, taking the experiment-specific polarization dependences into account.

While it is comparably simple to find a quantity proportional to the differential scattering cross section, an absolute value requires a proper evaluation of the integrated intensity. This is worked out in appendix A. As a result, the DMSCS per atom, $d\sigma_a/d\Omega$, can be calculated from the total integrated satellite intensity $I^{integr.}$ of the respective magnetic satellite by

$$\frac{d\sigma_a}{d\Omega} = \frac{I^{integr.}}{I_0} \frac{\sin\left(\widetilde{\Theta}_{Bragg}\right)}{\rho_{Ho} \cdot d \cdot L}, \tag{4.2}$$

where $\widetilde{\Theta}_{Bragg}$ is the Bragg angle of the magnetic satellite, I_0 is the intensity of the incident x-ray beam, $\rho_{Ho} = 3.2 \cdot 10^{-2}\,\text{Å}^{-3}$ is the atomic density of Ho metal, and d is the thickness of the Ho film. L denotes the so called Lorentz factor, which arises from the integration of the experimental data and ensures a proper normalization to an atomic value [67].

The DMSCS, as obtained from the integrated intensities of both satellites, are displayed in panel (b) of figure 4.7. Both the linear- and the circular-dichroic DMSCS reflect nicely their proportionality to the respective resonant oscillator strength - $(2F_0^1 - F_{+1}^1 - F_{-1}^1)^2$ for linear-dichroism and $(F_{-1}^1 - F_{+1}^1)^2$ for circular dichroism (see equation 2.10). The first weak increase of the circular-dichroic part at a photon energy of 1349eV corresponds to the small $\Delta J = 1$ (F_{-1}^1) component of the XAS. It increases to about $10^{-5}\,\text{Å}^2$ in the maximum of the $\Delta J = -1$ (F_{+1}^1) component, while a contribution of $\Delta J = 0$ (F_0^1) to the circular dichroic part can not be detected. The maximum of the linear dichroic DMSCS is by a factor of about 37 smaller than the maximum of the circular dichroic part; the former peaks at the $\Delta J = 0$ component of the XAS, referring to the resonant oscillator strength F_0^1. The other two components ($\Delta J = \pm 1$) contribute also to the linear-dichroic DMSCS and are visible as shoulders at the respective energies.

The absolute value of the atomic magnetic-scattering amplitude can be calculated by the square root of the DMSCS divided by the respective polarization factor P, since the DMSCS per atom can be written in general as $r_0^2 P^2 |f|^2$. With the polarization factors taken from equation 2.10, the absolute values of the circular- and linear-dichroic contributions to the magnetic-scattering amplitude could be determined as $200_{-0}^{+40}\, r_0$ and $160_{-0}^{+80}\, r_0$ respectively; see the respective resonance maxima in figure 4.7 (c). Even though the two values are measured at different positions in momentum space, they are comparable in magnitudes since they represent the amplitudes close to forward scattering due to comparably small scattering angles and the comparably long wave lengths in the soft x-ray regime ($\sin\Theta/\lambda \approx 0.024,\ 0.047$, respectively); in addition the form factor of resonant scattering shows in general a weak momentum dependence [83]. Systematic errors, which may arise from the deviations of the peak positions from forward scattering as well as from the temperature

dependence of the magnetic order would lead to an underestimation of the integrated intensity, and thus to a correction of the scattering amplitudes to slightly higher values. These first experimentally determined absolute values of the forward-scattering amplitudes are somewhat higher, but of the same order of magnitude as the theoretically estimated forward-scattering amplitude of $100\,r_0$ for dipole transitions at the $M_{IV,V}$ thresholds of the rare-earth elements, given by Hannon *et al.* [84].

A further reasonable way to quantify the resonant enhancement of the magnetic-scattering signal that does not depend on the specific magnetic structure, is the squared magnetic form factor divided by the value expected from non-resonant magnetic scattering at the same photon energy:

$$resonant\,enhancement = \frac{|f_{res.,mag.}|^2}{|f_{non-res.,mag.}|^2}.$$

$|f_{non-res.,mag.}|^2$ can be estimated from the fact that the non-resonant magnetic cross section of a single electron is reduced by a factor of $(h\nu/m_0c^2)^2$ compared to the cross section of charge scattering [67, 79]. The magnetic cross section is further reduced by a factor of N_m^2/N^2 that compares the number of magnetically active scattering electrons, N_m, with the total number of electrons per atom N. Thus, one can write [79]

$$|f_{non-res.,mag.}|^2 \approx \left(\frac{h\nu}{m_0c^2}\right)^2 \frac{N_m^2}{N^2}\,|f_{charge}|^2\,.$$

With the typical value of the atomic form factor, $f_{charge} \approx N = 67$, and $N_m^2/N^2 \approx 10^2/67^2$, an enhancement of the magnetic-scattering signal in the maximum of the resonance of about $5 \cdot 10^7$ is obtained. This huge resonant enhancement of the magnetic-scattering cross section and hence the huge contrast between magnetic-scattering and charge-scattering contributions in resonant soft x-ray scattering is exploited in the following parts of this dissertation to explore magnetic structures in ultrathin films.

4.3 Soft x-ray scattering vs. neutron scattering

Whereas the previous section dealt with the satellite intensity at a given low temperature in a magnetically well-ordered state, a knowledge of the precise relationship between the satellite intensity and the magnetic order parameter is important for quantitative studies, as discussed in the following. The proportionality between non-resonant and resonant magnetic scattering intensities at the Ho L_{III} absorption threshold was established for the first-order satellite of bulk Ho metal by Gibbs *et al.* [101]. Helgesen *et al.* found at the L_{III} resonance equal power-law behavior for the integrated intensities of the first-order magnetic satellites of a bulk Ho sample and a 2-μm-thick Y-bound Ho film, with a critical exponent that was in good agreement with the results obtained by earlier neutron scattering experiments [73]; this confirmed that resonant scattering at this resonance is indeed probing the squared magnetic order parameter. The exponents obtained from the

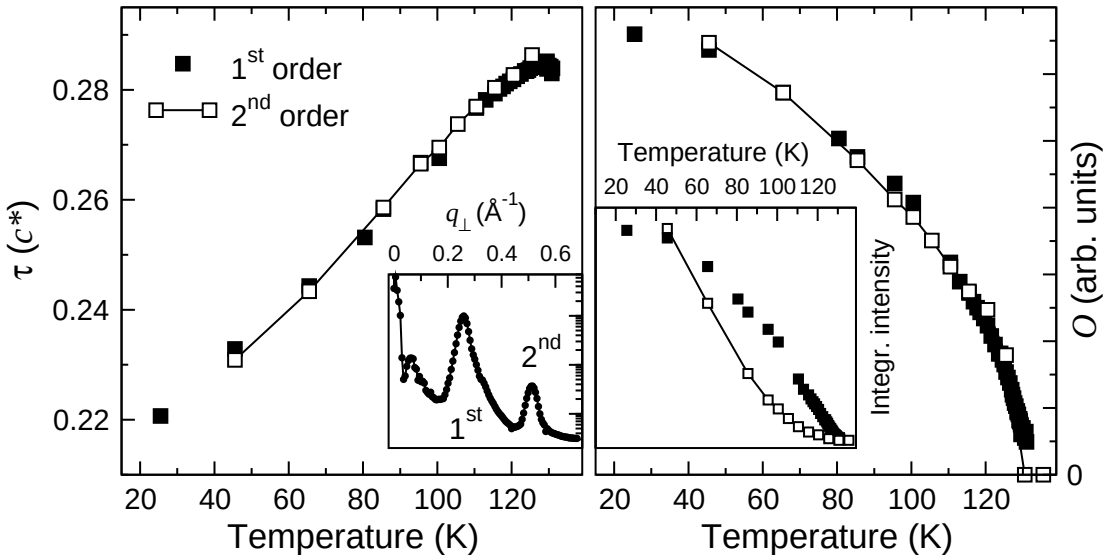

Figure 4.8: Comparison of the magnetic modulation vector (left panel) and the magnetic order parameter (right panel) as a function of temperature obtained from the first- and second-order satellite of an 89-ML Ho film. The inset in the right panel shows the direct comparison of the integrated intensities.

second-order and third-order magnetic satellites of the bulk sample, however, were found to be not simple integer multiples of the ones derived from the first-order satellite as one would expect from mean-field theory. Since the resonant scattering mechanisms at the Ho L_{III} and M_V thresholds are of different origin (see section 2.2), the results for the L_{III} resonance cannot be applied directly to the soft x-ray resonance.

The classical method for magnetic structure studies is neutron scattering. There are fundamental and practical differences between neutron scattering and resonant magnetic x-ray scattering, since both techniques probe the magnetic structure in different ways. Neutron scattering is known to be sensitive to the magnetization density [123,124], why the method directly measures the order parameter of the magnetic system. Resonant magnetic x-ray scattering, on the other hand, probes the orientation of the local magnetic moment [83], as can be seen from equation 2.9. Thus, the question arises how the quantity probed by resonant magnetic scattering is related to macroscopic quantities like the magnetization density. Since diffraction experiments are sensitive to collective order rather than to local properties, resonant magnetic x-ray diffraction probes the collective orientation of the local magnetic moments; in this way it may provide access to the magnetic order parameter. It is therefore instructive to compare the two methods on the same sample, neutron and magnetic x-ray scattering.

The scattering amplitude in equation 2.9 contains the local magnetic axis as a linear term for the first-order, and as a quadratic dependence for the second-order contribution. Since the measured intensity is proportional to the square of the scattering amplitude, it

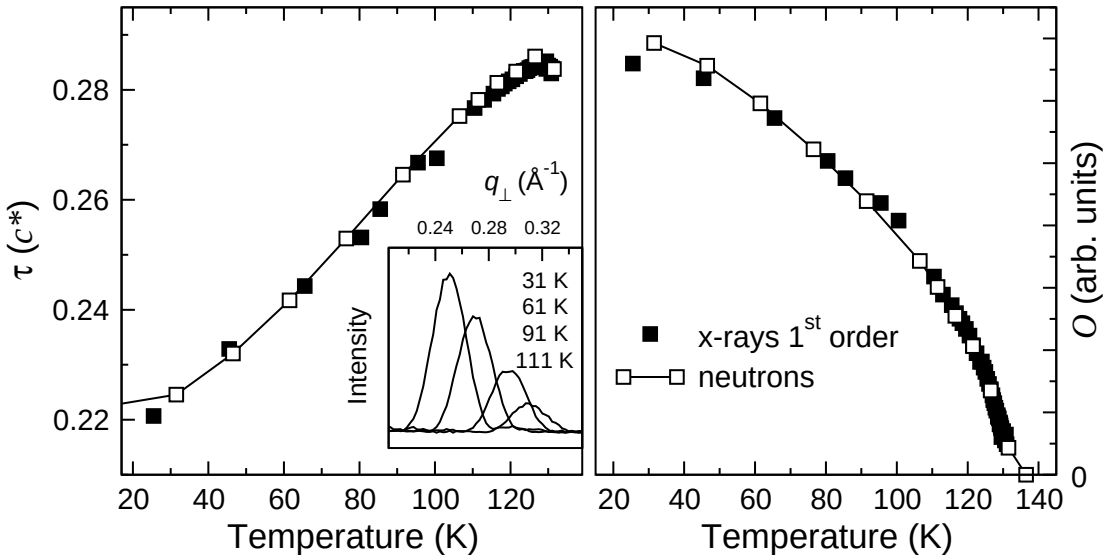

Figure 4.9: Comparison of the information obtained from magnetic soft x-ray scattering and neutron scattering. The data were recorded from the same sample. The left panel shows the magnetic modulation vector τ and the right panel the order parameter, O, obtained from a 89-ML Ho film as a function of temperature. Open squares are measured by neutron scattering, filled squares by x-rays at the M_V resonance. The inset shows raw data from neutron scattering.

can be expected that the order parameter O is given by

$$O\,(T) \propto I_{fo}^{1/2}\,(T)\;\;;\quad O\,(T) \propto I_{so}^{1/4}\,(T)\,, \tag{4.3}$$

where I_{fo} and I_{so} are the integrated intensities of the first- and second-order satellite, respectively, consistent with a mean-field scaling [73].

To prove this, the temperature dependences of the two magnetic satellites were measured for a 89-ML MBE-grown Ho film. The left panel in figure 4.8 shows the temperature dependence of the magnetic modulation vector directly determined from the respective peak position. Despite the quite different scattering angles, both dependences are identical even without dispersion correction, because the real part δ of the index of refraction is close to zero at the resonance maximum (figure 4.4 (b)). Also the magnetic order parameter O, calculated from the integrated intensities of the two satellites according to equations 4.3, shows a very similar behavior, different from the respective integrated intensities, which are displayed in the inset. Because of the large film thickness and the different detection angles for the two satellites, an absorption correction is required for the comparison. To check whether these temperature dependences are proportional to the order parameter, the same sample was studied by neutron scattering.

Figure 4.9 shows a comparison of the temperature dependences of the magnetic modulation vector τ and the order parameter O obtained from the Ho(000+τ) magnetic satellite by neutron scattering and resonant soft x-ray scattering. The data were recorded on the

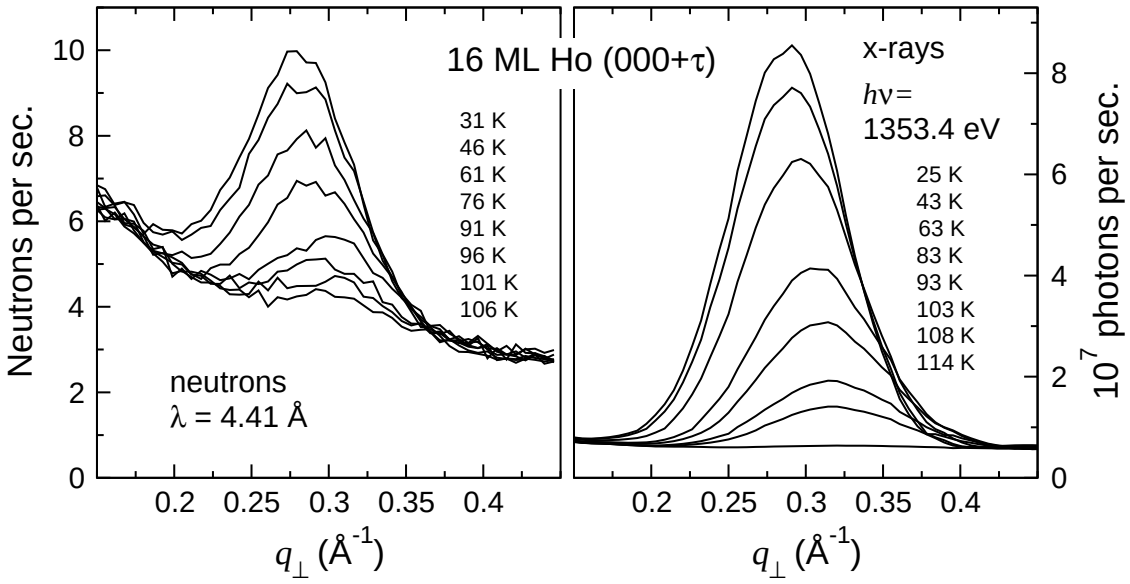

Figure 4.10: Comparison of magnetic soft x-ray scattering and neutron scattering data, recorded from the same 16-ML Ho film. The spectra on the left panel were measured by neutron scattering at various temperatures with a total counting time of 510 s per data point. On the right panel, data measured with soft x-rays at the M_V resonance maximum are displayed. The total counting time per data point was about 1 s.

same sample with a thickness of 89 monolayers. The neutron-scattering experiments were performed by Vincent Leiner in the group of Prof. Zabel on the *ADAM* reflectometer at the *Institut Laue-Langevin* (ILL) in Grenoble, France, using unpolarized neutrons with a wavelength of 4.41 Å. The temperature dependences of both, the magnetic modulation vector (left panel of figure 4.9) and the order parameter (right panel) obtained from neutron (open symbols) and resonant magnetic soft x-ray scattering (filled symbols) are identical. This is a strong indication that the informations on magnetic order obtained from both methods are equivalent.

A complementary aspect of x-ray scattering as compared to neutron scattering arises from the different penetration depths. Neutron scattering is a really bulk sensitive method, able to measure the entire volume of the sample. X-rays, on the other hand, are restricted to the "near-surface" region also in the non-resonant case, entering only a few micrometers into the target. At a strong resonance, like the M_V threshold, strongly reduced probing depths can be observed even in films of a few monolayers thickness as discussed in the previous sections. This reduced probing depth, on the other hand, is an advantage, when thin films are studied. Together with the high intensity of the 3^{rd}-generation synchrotron-radiation sources it allows us to study thin films with reasonable statistics in a reasonable time. This is demonstrated in figure 4.10. The left panel displays neutron diffraction spectra of the Ho(000+τ) magnetic satellite from a 16-ML film. With a counting rate of less than 6 neutrons per second on a nuclear-scattering background of about 4 neutrons

per second, one data point required a total counting time of 510 s. The data quality of the high-temperature spectra, still ≈ 9 K below the ordering temperature, do not allow detailed analysis. Soft x-ray scattering at the maximum of the M_V resonance from the same sample results in a counting rate of the order of 10^7 photons per second and allows to record a complete spectrum within seconds. With such good statistics, it is possible to perform a detailed analysis even around the critical temperature of films of only a few monolayer thickness, which will be used in the next chapter.

There are other interesting differences between these techniques, like the spectroscopic information obtained in resonant soft x-ray scattering by using different parts of the resonance, which has no counterpart in neutron scattering.